



# CHORUS

This is the accepted manuscript made available via CHORUS. The article has been published as:

## Low energy scattering cross section ratios of $^{14}\text{N}(p,p)^{14}\text{N}$

R. J. deBoer, D. W. Bardayan, J. Görres, P. J. LeBlanc, K. V. Manukyan, M. T. Moran, K. Smith, W. Tan, E. Uberseder, M. Wiescher, P. F. Bertone, A. E. Champagne, and M. S. Islam

Phys. Rev. C **91**, 045804 — Published 20 April 2015

DOI: [10.1103/PhysRevC.91.045804](https://doi.org/10.1103/PhysRevC.91.045804)

# Low energy scattering cross section ratios of $^{14}\text{N}(p, p)^{14}\text{N}$

R. J. deBoer,<sup>\*</sup> D. W. Bardayan, J. Görres, P. J. LeBlanc, K. V. Manukyan,  
M. T. Moran, K. Smith,<sup>†</sup> W. Tan, E. Überseder,<sup>‡</sup> and M. Wiescher  
*The Joint Institute for Nuclear Astrophysics, Department of Physics,  
University of Notre Dame, Notre Dame, Indiana 46556 USA*

P. F. Bertone<sup>§</sup> and A. E. Champagne  
*Department of Physics, University of North Carolina at Chapel Hill, Chapel Hill, North Carolina 27599 USA and  
Triangle Universities Nuclear Laboratory, Durham, North Carolina 27708 USA*

M. S. Islam  
*Department of Physics and Astronomy, Ball State University, Muncie, Indiana 47306 USA*

**Background** The slowest reaction in the first CNO cycle is  $^{14}\text{N}(p, \gamma)^{15}\text{O}$ , therefore its rate determines the overall energy production efficiency of the entire cycle. The cross section presents several strong resonance contributions, especially for the ground state transition. Some of the properties of the corresponding levels in the  $^{15}\text{O}$  compound nucleus remain uncertain, which affects the uncertainty in extrapolating the capture cross section to the low energy range of astrophysical interest.

**Purpose** The  $^{14}\text{N}(p, \gamma)^{15}\text{O}$  cross section can be described using phenomenological  $R$ -matrix. Over the energy range of interest, only the proton and  $\gamma$ -ray channels are open. Since resonance capture makes significant contributions to the  $^{14}\text{N}(p, \gamma)^{15}\text{O}$  cross section, resonant proton scattering data can be used to provide additional constraints on the  $R$ -matrix fit of the capture data.

**Methods** A 4 MV KN Van de Graaff accelerator was used to bombard protons onto a windowless gas target containing enriched  $^{14}\text{N}$  gas over the proton energy range from  $E_p = 1.0$  to 3.0 MeV. Scattered protons were detected at  $\theta_{\text{lab}} = 90, 120, 135, 150,$  and  $160^\circ$  using ruggedized silicon detectors. In addition, a 10 MV FN Tandem Van de Graaff accelerator was used to accelerate protons onto a solid Adenine target, of natural isotopic abundance, evaporated onto a thin self-supporting carbon backing, over the energy range from  $E_p = 1.8$  to 4.0 MeV. Scattered protons were detected at 28 angles between  $\theta_{\text{lab}} = 30.4$  and  $167.7^\circ$  using silicon photodiode detectors.

**Results** Relative cross sections were extracted from both measurements. While the relative cross sections do not provide as much constraint as absolute measurements, they greatly reduce the dependence of the data on otherwise significant systematic uncertainties, which are more difficult to quantify. The data are fit simultaneously using an  $R$ -matrix analysis and level energies and proton widths are extracted. Even with relative measurements, the statistics and large angular coverage of the measurements result in more confident values for the energies and proton widths of several levels in particular the broad resonance at  $E_{cm} = 2.21$  MeV, which corresponds to the  $3/2^+$  level at  $E_x = 9.51$  MeV in  $^{15}\text{O}$ . In particular the  $s$  and  $d$  wave angular momentum channels are separated.

**Conclusion** The relative cross sections provide a consistent set of data that can be used to better constrain a full multichannel  $R$ -matrix extrapolation of the capture data. It has been demonstrated how the scattering data reduce the uncertainty through a preliminary Monte Carlo uncertainty analysis, but several other issues remain that make large contributions to the uncertainty, which must be addressed by further capture and lifetime measurements.

PACS numbers: Valid PACS appear here

## I. INTRODUCTION

Hydrogen burning in stars more massive than our sun is dominated by the CNO cycles. The least efficient reaction determines the overall rate of the cycle, and for the CN cycle, this reaction is  $^{14}\text{N}(p, \gamma)^{15}\text{O}$ . This makes its reaction rate at stellar temperatures the most critical

nuclear physics input parameter for modeling the cycle.

Recent solar neutrino measurements have reached unprecedented levels of sensitivity, obtaining measurements of the  $^8\text{B}$ ,  $^7\text{Be}$ , and  $pp$  neutrino fluxes to 3% [1], 5% [2], and 11% [3] overall uncertainties respectively. With the capability of precision flux measurements and a firm theoretical understanding of weak interactions, precision solar neutrino measurements stand ready to test the limitations of the standard solar model (SSM) [4]. In particular, these measurements provide a new and independent tool for determining the solar metallicity of our sun through measurements of the CNO neutrino fluxes. It has been estimated that SNO+ can measure the flux of  $^{15}\text{O}$  neutrinos with an uncertainty level of 7% with three years of running [4]. On the SSM side, the largest source of uncertainty is the cross section of  $^{14}\text{N}(p, \gamma)^{15}\text{O}$ , which

<sup>\*</sup>Electronic Address: rdeboer1@nd.edu

<sup>†</sup>Present address: Department of Physics and Astronomy, University of Tennessee Knoxville, Knoxville, Tennessee 37996 USA

<sup>‡</sup>Present address: Department of Physics and Astronomy, Texas A&M University, College Station, TX 77843 USA

<sup>§</sup>Present address: NASA George C. Marshall Space Flight Center, Huntsville, AL 35812



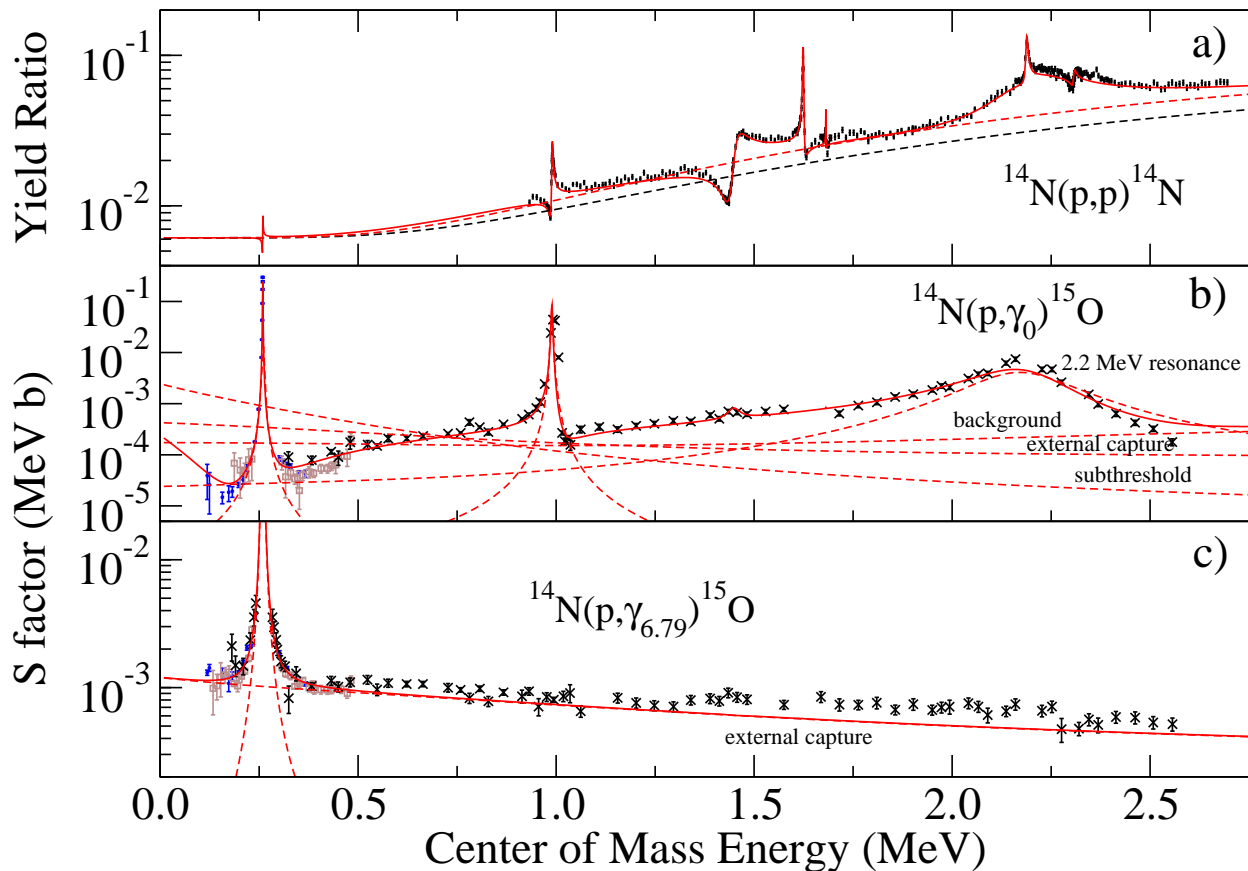


FIG. 2: (Color online) Example simultaneous  $R$ -matrix fits to elastic scattering (this work), ground state and 6.79 MeV capture data [11] (solid blue), [10] (brown open squares), [19] (black crosses), illustrating the connection of the 6.79 MeV ANC to each channel, the complexity of the ground state, and the relative simplicity of the 6.79 MeV primary transition. Throughout the figure the solid red line represents the  $R$ -matrix fit, which has been performed to the three channels simultaneously. Fig 2 a) shows an example of the scattering data yield ratios reported in this work ( $\frac{d\sigma/d\Omega_{160^\circ}}{d\sigma/d\Omega_{30^\circ}}$ ). The black dashed line represents pure hard sphere Coulomb scattering with angular momentum truncated at  $l = 7$ . The red dashed line represents the Coulomb scattering and the 6.79 MeV subthreshold state. Fig 2 b) shows the fit to the ground state capture data. The low energy region is a complicated mixture of the contributions from the low energy tail of the  $3/2^+$   $E_{cm} = 2.21$  MeV resonance, background contributions from higher lying  $3/2^+$  resonances, ground state external capture, and the 6.79 MeV subthreshold state. Fig 2 c) shows the capture to the 6.79 MeV state where the cross section is dominated by external capture and the single narrow resonance at  $E_{cm} = 259$  keV.

important constraints on the reaction mechanism. In this paper, we report on a new measurement of  $^{14}\text{N}(p,p)^{14}\text{N}$  over a wide angular range and in the energy range of interest for the  $^{14}\text{N}(p,\gamma)^{15}\text{O}$  reaction. Although several previous elastic scattering experiments are reported in the literature, their results are often inconsistent, yielding differences in absolute cross-section scales, energy calibration, and sometimes even energy dependence [12, 13]. Part of these discrepancies may be the result of poor target stability since solid Nitrogen compounds used for transmission targets are often unstable under long term bombardment, making the extraction of absolute cross sections very challenging. A substantial amount of the target effects are avoided by analyzing the relative yields of the measurements instead. This technique has proved very useful for the  $R$ -matrix analysis of the  $^{12}\text{C}+\alpha$  reac-

tions [21].

In Sec. II the details of the experiments are presented. This is followed by a description of the extraction of the yield ratios and the  $R$ -matrix analysis in Sec. III. A discussion of the data is given in Sec. IV and a summary is given in Sec. V.

## II. EXPERIMENT AND RESULTS

Two complementary experimental setups were employed for the measurements. The first setup utilized an accelerator that could reach low energies and used a windowless gas target, which provided a nearly contaminant free background but only allowed for measurements at a few angles. The second setup allowed for detailed angular

distributions, but was constrained by an accelerator that could not reach as low in energy. Additionally, the solid self-supporting target had impurity peaks arising from the backing material and the solid nitrogen compound that was used.

The first measurements were made over a low energy range from  $E_p = 1.0$  to  $3.0$  MeV. The proton beam was supplied by a 4 MV KN Van de Graaff accelerator at the University of Notre Dame's Nuclear Science Laboratory (NSL). Beam currents were of the order of a few hundred nA. The energy calibration of the Van de Graaff was established to better than 1 keV using the well known  $^{27}\text{Al}(p, \gamma)^{28}\text{Si}$  resonance at 0.992 MeV [22]. For this setup the windowless gas target system RHINOCEROS [23] was used. This gas target has been used extensively in the past and is very well characterized (see e.g. Refs. [24, 25] and references therein). Nitrogen gas, depleted in  $^{15}\text{N}$  and kept at a pressure of  $\sim 0.25$  Torr, was used throughout the experiment. This corresponds to a target thickness of  $\approx 0.5 \mu\text{g}/\text{cm}^2$ . The target chamber was very similar to the one shown in Fig. 2a of Ref. [25], except that additional view ports were available at  $\theta_{\text{lab}} = 135, 150, \text{ and } 165^\circ$ . Ruggedized silicon photodiode detectors were mounted at  $\theta_{\text{lab}} = 30, 90, 105, 135, 150, \text{ and } 165^\circ$  approximately 6 cm from the center of the gas target. The uncertainty in the laboratory angle is estimated to be  $0.5^\circ$  based on the uncertainty in the geometry. Because of the high purity target, no contaminant peaks were observed, giving very clean yield spectra.

For the second measurement, a proton beam of energy from  $E_p = 1.8$  to  $4.0$  MeV was supplied by the 10 MV FN Tandem Van de Graaff accelerator at the NSL. The accelerator's energy calibration was verified to  $\approx 2$  keV using well known narrow resonances in the  $^{12}\text{C}(\alpha, \alpha)^{12}\text{C}$  reaction [21]. The target was an  $\approx 20 \mu\text{g}/\text{cm}^2$  thick layer of Adenine ( $\text{C}_5\text{H}_5\text{N}_5$ ) of natural isotopic abundance evaporated on a carbon backing foil, also of natural abundance and of similar thickness. The target was mounted at  $35^\circ$  relative to the horizontal beam axis on an electrically isolated target ladder. The angle was chosen to minimize energy straggling of the scattered particles and to prevent the target ladder from blocking line of sight to any of the detectors. Beam currents were kept below 300 nA in an effort to avoid rapid target degradation. A 76 cm (30") radius scattering chamber housed the detector array. The scattering chamber contains a rotating table for detector mounting and alignment. Using a fixed telescope and the rotating table, the detector angles were found to be reproducible to  $0.1^\circ$ . The table is equipped with fixed mounting positions for the detectors, allowing for accurate reproducibility of the detector to target distance. The radial distance of the detectors to the target were determined to 0.1 cm. As the geometric setup is critical for the analysis, uniformity of the detector setup was checked by comparing with Rutherford scattering from gold at  $E_\alpha = 6.575$  MeV, placing a mixed  $\alpha$  source at the target position, and by comparing  $^{12}\text{C}(\alpha, \alpha)^{12}\text{C}$  angular distributions with those of Ref. [26]. The overall

setup is very similar to that described in Ref. [21] and a schematic diagram is shown in Fig. 3.

The detector array consisted of 28  $1 \text{ cm} \times 1 \text{ cm}$  Hamamatsu photodiodes. The detectors were mounted with  $0.625(6) \text{ cm}$  ( $1/4''$ ) diameter collimators. The uniformity of the collimator sizes were determined to be within 1.1% by making measurements using a fixed geometric setup and a radioactive  $\alpha$  source. The detectors were placed  $37.6(1) \text{ cm}$  from the target at backward angles and at  $59.8(1) \text{ cm}$  at forward angles. The difference in distance helped to mitigate the high count rate at very forward angles. Two detectors were placed symmetrically across the beam axis at  $\theta_{\text{lab}} = 94.3^\circ$  in order to monitor the effect of changes in the position of the beam spot on the target. The detectors had an energy resolution of  $\approx 20$  keV, allowing for separation of the scattering peaks from the contaminant reactions. Observed contaminant peaks were from  $^{12}\text{C}$  and  $^{13}\text{C}$  in the natural isotopic backing and target material and  $^{16}\text{O}$  absorbed in the backing.

Because of the limited resolution of the silicon detectors, the scattering peaks from  $^{14}\text{N}$  could not always be separated from the  $^{12}\text{C}$ ,  $^{13}\text{C}$ , and  $^{16}\text{O}$  peaks depending on the incoming proton beam energy and detector angle. Of critical importance for the analysis is that the  $^{14}\text{N}$  scattering peak can always be separated from the contaminant peaks at the most backward angle of  $\theta_{\text{lab}} = 167.7^\circ$ . This was observed to be possible down to the lowest energy of  $E_p = 1.8$  MeV. For each run a background run was also measured using a blank carbon foil backing of similar thickness.

The Adenine target material has a relatively low melting point of  $360^\circ \text{ C}$ . Over the course of the experiment the target was monitored by repeatedly scanning over the narrow  $^{14}\text{N}(p, p)^{14}\text{N}$  resonance at  $E_p = 3.19$  MeV ( $\Gamma = 3(1) \text{ keV}$ ) [20]. No change in the peak position was observed from Carbon build up, but the yield decreased substantially. About 50% of the initial target material was lost over the course of the experiment.

### III. ANALYSIS

Because of past problems with absolute cross section measurements, this analysis extracts the ratio of the experimental yields. For reactions with strong anisotropic resonance transitions, differential yield ratios can provide strong constraints on the level parameters when analyzed in a reaction framework like  $R$ -matrix (see, e.g., Ref. [21]). Further, the target thickness approximately cancels in the yield ratio greatly reducing what is often one of the largest sources of systematic uncertainty. While not as critical for the current measurement, the integrated charge can also be difficult to measure accurately, especially if higher  $Z$  beam particles are used. The remaining uncertainties, when the reaction peaks are cleanly separable, are then largely from statistics and from geometric quantities. For example, the solid angles of the detectors, which can usually be measured to high

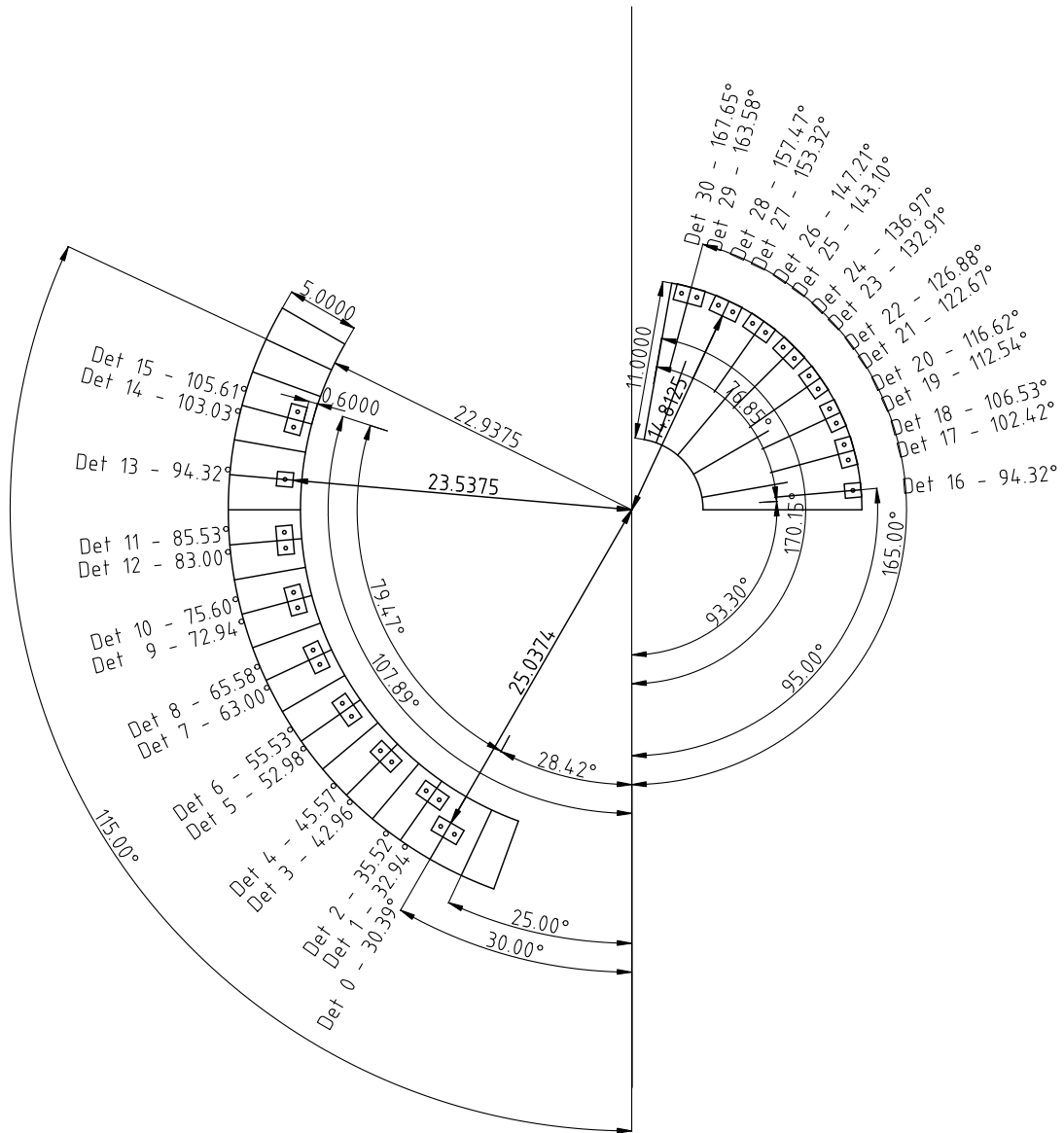


FIG. 3: Schematic of the detection setup for the higher energy solid target measurements.

precision.

Given the good approximation that the change in the differential cross section as a function of energy is small compared to the energy loss of the beam particles through the target material, thin-target approximations can be used in the analysis. The effective energy of the beam was calculated using the approximation  $E_{\text{eff}} = E_p - \Delta E/2$ , where  $\Delta E$  is the energy loss through the thin target. The differential yield observed for a given reaction peak in the energy spectrum is given approximately by

$$dY \approx N_b N_t \epsilon \left( \frac{d\sigma}{d\Omega} \right) d\Omega. \quad (1)$$

where  $N_b$  is the total number of beam particles incident on the target,  $N_t$  is the number of active target atoms per unit area,  $\epsilon$  is the efficiency, and  $d\Omega$  is the solid angle subtended by an individual detector. Since several detectors were employed, each of the differential yields were measured simultaneously. As a result,  $N_b$  and  $N_t$  are the same for each angle at a given energy. Then the ratio of the yields at angle 1 to angle 2 is

$$\begin{aligned} \frac{dY_1}{dY_2} &\approx \frac{N_b N_t (d\sigma/d\Omega)_1 d\Omega_1 \epsilon_1}{N_b N_t (d\sigma/d\Omega)_2 d\Omega_2 \epsilon_2} \\ &\approx \frac{(d\sigma/d\Omega)_1 d\Omega_1 \epsilon_1}{(d\sigma/d\Omega)_2 d\Omega_2 \epsilon_2}. \quad (2) \end{aligned}$$

As the detector efficiencies and solid angles have all been determined, the cross section ratios can be extracted.

For the gas target setup, the pure  $^{14}\text{N}$  gas ensured that the spectra had very little background and the extraction of the yields was straightforward. A forward detector at  $\theta_{\text{lab}} = 30^\circ$  was used as the normalization detector. The ratio of the yields of the other detectors relative to this one are shown in Fig. 4.

For the solid target setup, the extraction of the  $^{14}\text{N}$  yields was complicated by the presence of the contaminant peaks from  $^{12}\text{C}$ ,  $^{13}\text{C}$ , and  $^{16}\text{O}$ . For each run a background run was also performed using a blank carbon backing that contained all of the contaminant nuclei observed in approximately the same stoichiometry. The main contaminant peak was  $^{12}\text{C}$ , which often had a yield several times that of the  $^{14}\text{N}$  peak. The  $^{13}\text{C}$  and  $^{16}\text{O}$  peaks were only small contaminants, estimated to be less than 2% of the yield of the  $^{14}\text{N}$  peak over the entire energy range.

The relative  $^{14}\text{N}$  yields were extracted using two different techniques. If the  $^{14}\text{N}$  peak could be clearly separated from the other scattering peaks, its yield was extracted directly. This was often the case for backward angle detectors (i.e.  $\theta_{\text{lab}} > 90^\circ$ ). If the  $^{14}\text{N}$  peak and a contaminant peak overlapped, a subtraction method was used. For each of the runs at each energy, the background run was first normalized to the Adenine target run using the  $^{12}\text{C}$  peak yields in the most backward angle detector

( $\theta_{\text{lab}} = 167.65^\circ$ ) where all of the scattering peaks were always resolvable as demonstrated in Fig. 5. The spectra at each angle were then subtracted from each other in order to obtain the  $^{14}\text{N}$  yield. The  $^{14}\text{N}$  yield, determined through either method, was then divided by the  $^{14}\text{N}$  yield of the most backward angle detector to obtain the relative yields. To check the consistency of the method the background subtraction was implemented even when the peaks could be separated. A comparison of the yield ratios resulting from the two techniques is shown in Fig. 6.

To monitor the effect of the beam spot position on the target, two detectors were placed at the same angle,  $\theta_{\text{lab}} = 94.32^\circ$ , but on opposite sides of the target as shown in Fig. 7. The yield ratios were found to be in good agreement indicating that effects from changes in the beam spot position were negligible compared to the statistical uncertainties.

The differential cross sections and yield ratios are fit simultaneously in an  $R$ -matrix framework using the code AZURE2 [27]. The analysis used a channel radius of 4.2 fm and a maximum orbital angular momentum of  $l = 7$ . The parameterization of Ref. [28] has been used so that widths from the literature may be used as starting parameters for the fit. Starting values for the level parameters ( $J^\pi$ ,  $E$ ,  $\Gamma_p$ ) have been taken from the compilation [20]. Fig. 1 shows the levels that were considered in the analysis. Narrow resonances have been neglected. Figs. 4 and 7 show the fits to the data from the gas target measurement and the solid target setup respectively. The fits were performed to all the data simultaneously. Table I lists the final values of the level parameters from the  $R$ -matrix fit.

Because of the quantity of data, the statistical uncertainties of the derived level parameters are usually quite small. Even though the statistical uncertainties from the solid target measurements are rather large on a point to point basis, owing to the background subtraction, this is compensated by the many angles of measurement. The statistical uncertainties were calculated using the routine MINOS, available as part of MINUIT2 analysis package [29]. Uncertainties at a  $1\sigma$  level were determined using a value of  $\Delta\chi^2 = \sqrt{\chi^2/N}$  [30] where the best fit yielded a value of  $\chi_{\text{min}}^2/N = 2.34$  for 4614 data points. The systematic uncertainties on the energies come chiefly from the uncertainty in beam energy, the target thickness, and the  $R$ -matrix model. The uncertainties in energy and target thickness are approximately constant over the range of each of the experimental measurements while the model uncertainties vary depending on the resonance. For the partial widths of the resonances, the model uncertainties from the  $R$ -matrix analysis often dominate. The full listing of all the uncertainties considered is given in Table I.

The uncertainties in the parameters are also sensitive to the value of the adopted channel radius. An initial channel radius of 5.5 fm was used, based on similar radii that were adopted for the analysis of  $^{14}\text{N}(p, \gamma)^{15}\text{O}$  data (e.g. Refs. [9–11, 31]). A preliminary fit was obtained using a value of 5.5 fm but subsequent sensitivity studies

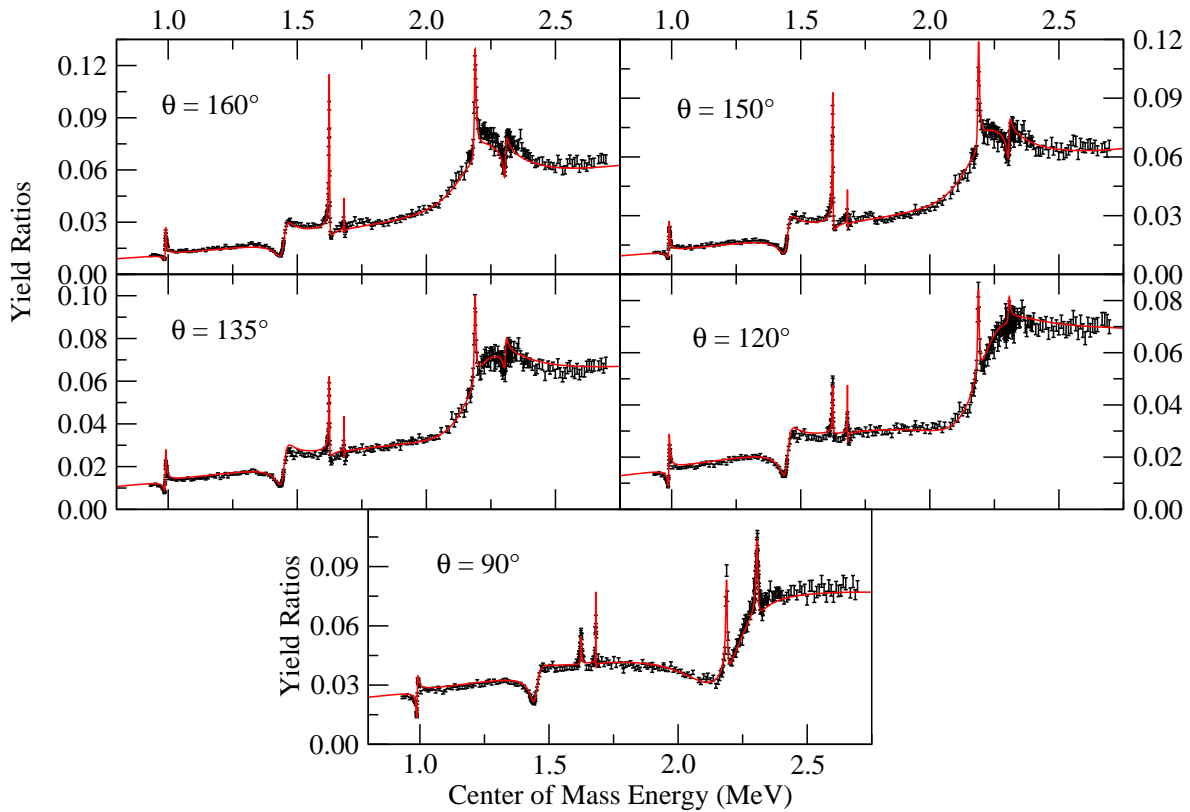


FIG. 4: (Color online) Yield ratios of the  $^{14}\text{N}(p,p)^{14}\text{N}$  reaction measured using a gas target setup. The reference angle is  $\theta_{\text{lab}} = 30^\circ$ . Uncertainties are statistical only. The solid red line indicates the  $R$ -matrix fit.

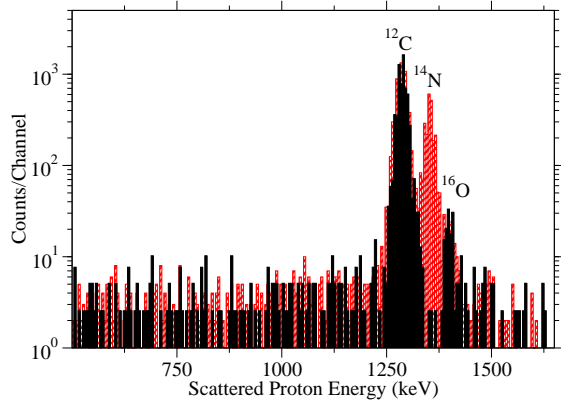


FIG. 5: (Color online) Spectra for the lowest beam energy ( $E_p = 1.8$  MeV) at the most backward angle ( $\theta_{\text{lab}} = 167.7^\circ$ ). The red hashed histogram represents the Adenine run and the black filled histogram the background run with a carbon foil only. The spectra have been normalized to each other using the areas of the carbon peaks.

found that the fit preferred a smaller channel radius of 4.2 fm. Further, compared to the value of  $\Delta\chi^2$  adopted for the rest of the uncertainty analysis a range of only  $4.2 \pm 0.1$  fm was found to be within this range. It is interesting to note that this smaller value of the channel

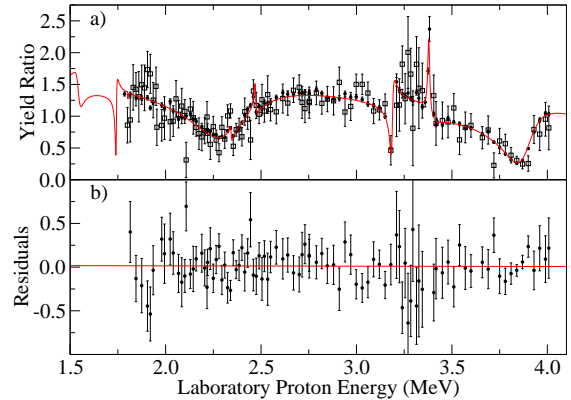


FIG. 6: (Color online) Fig. 6 a) shows a comparison of the yield ratio at  $\theta_{\text{lab}} = 112.5^\circ$  to the most back angle detector at  $\theta_{\text{lab}} = 165.7^\circ$  obtained for separately resolved  $^{14}\text{N}$  and  $^{12}\text{C}$  scattering peaks (black circles) to when the background subtraction method is used (open squares). The red solid line represents the  $R$ -matrix fit, which is shown to guide the eye. In Fig. 6 b) the difference between the separately resolved peak yields and those from the subtraction method are shown. The expectation is that the average value should be zero. A linear fit was performed resulting in  $\Delta y = -0.004E_p + 0.023$  with  $\chi^2 = 79.7$  (97 data points). Setting the slope and intercept parameters to zero yields a  $\chi^2$  of 80.1 and a corresponding  $\Delta\chi^2 = 0.4$ , within  $1\sigma$  uncertainty ( $\Delta\chi^2 < 1$ ).



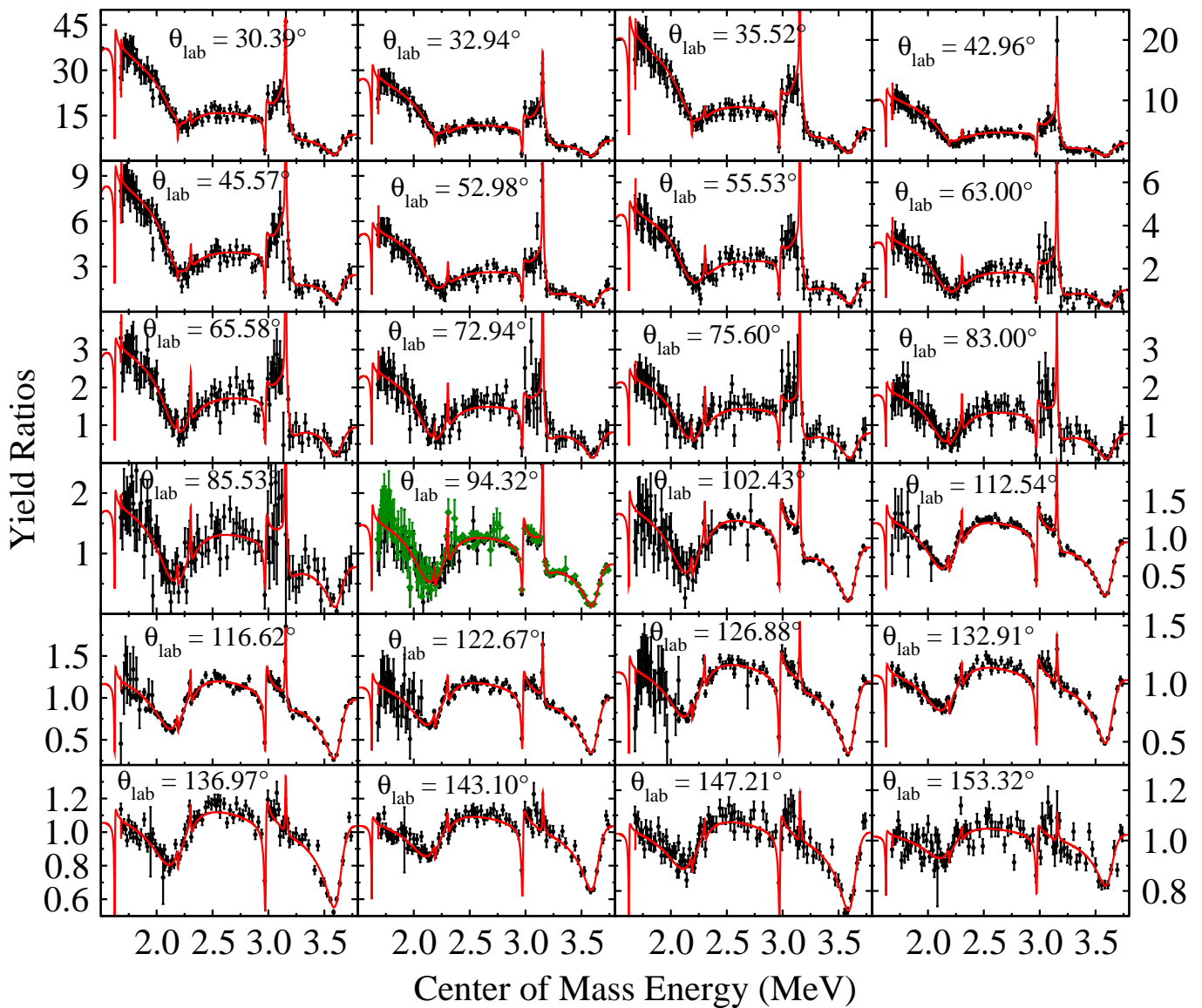


FIG. 7: (Color online) Yield ratios of the  $^{14}\text{N}(p,p)^{14}\text{N}$  reaction measured using a solid target setup. The reference angle is  $\theta_{\text{lab}} = 167.65^\circ$ . Uncertainties are statistical only. The solid red line indicates the  $R$ -matrix fit. The yield ratio curve at  $\theta_{\text{lab}} = 94.32^\circ$  compares the results from the two detectors at the same angle but on opposite sides of the beam as denoted by the black circular points and green diamond points for the closer distance of 37.6(1) cm and the farther distance of 59.8(1) cm respectively.

radius is consistent with the one obtained in Ref. [5] (4.14 fm) for the best fit to the  $E_x = 6.79$  MeV transition. The uncertainty in the level parameters arising from this range of radius can be quite significant and is reflected in the model uncertainties listed in Table I.

#### IV. DISCUSSION

Several resonances are observed over the proton bombarding energy range from  $E_{cm} = 0.90$  to 3.75 MeV. This analysis concentrates on the broad resonance structures that may have an effect on the extrapolation of

the  $^{14}\text{N}(p,\gamma)^{15}\text{O}$  cross section to astrophysical energies, especially for the ground state transition. Of particular interest is the broad resonance at  $E_{cm} = 2.21$  MeV, which corresponds to the  $3/2^+$  level at  $E_x = 9.51$  MeV in  $^{15}\text{O}$  and the branching of its width into  $l = 0$  and 2 channels. The importance of this level and its branching has been highlighted in Refs. [9, 19, 31] for example. This level can be populated through three possible channels depending on the coupling of the channel spin ( $s$ ) and orbital angular momentum ( $l$ ):  $(s, l) = (\frac{3}{2}, 0)$ ,  $(\frac{1}{2}, 2)$ , and  $(\frac{3}{2}, 2)$ . The  $R$ -matrix fit finds that both  $l = 0$  and 2 channels are required. A good fit can be obtained using only the  $(\frac{3}{2}, 0)$  and  $(\frac{1}{2}, 2)$  channels, but since the angular

TABLE I: Level parameters extracted from the  $R$ -matrix fit to the scattering data. A channel radius of 4.2 fm was used and the parameterization of Ref. [28] is used to fit physical parameters directly. Partial widths are given in the center of mass frame. Energies of subthreshold states were fixed at the values given in the compilation [20], ANCs are fixed to those given in Ref. [17] after changing from an  $(l, j)$  to an  $(s, l)$  coupling scheme. Uncertainties are of the form (statistical, systematic, model). **Fitted parameters are given in bold font.** In some cases multiple channels are allowed for the same  $l$ . In most cases only one of these channels was necessary, hence some possible channels are omitted.

$J^\pi$	this work		literature		this work		literature	
	$E_x$ (MeV)		$l$	$s$	$\Gamma$ (keV)	or ANC ( $\text{fm}^{-1/2}$ )		
$\frac{1}{2}^-$	0	-	1	0.5	-		0.23(1)	
			1	1.5	-		7.4(4)	
	15	-	1	0.5	<b><math>4.2(10,40,1) \times 10^3</math></b>		-	
	-	-	1	1.5	<b><math>5.5(20,10,5) \times 10^3</math></b>		-	
$\frac{1}{2}^+$	-	5.183(1)	0	0.5	-		0.33(6)	
	-	7.5565(4)	0	0.5	-		0.99(10)	
	<b>8.7501(3,10,3)</b>	8.743(6)	0	0.5	<b>37.1(2,8,2)</b>		32	
	15	-	0	0.5	<b><math>7.3(16,38,7) \times 10^3</math></b>		-	
$\frac{3}{2}^-$	-	6.1763(17)	1	0.5	-		0.47(3)	
	-	-	1	1.5	-		0.53(3)	
	<b>9.6041(2,10,1)</b>	9.609(2)	1	0.5	<b>0.87(3,3,1)</b>		8.8(5)	
	-	-	1	1.5	<b>10.6(4,4,1)</b>		-	
	<b>10.4519(8,20,26)</b>	10.48	1	0.5	<b>16.5(7,39,1)</b>		25(5)	
	-	-	1	1.5	<b>1.8(6,7,1)</b>		-	
	15	-	1	0.5	<b><math>0.40(2,1,16) \times 10^3</math></b>		-	
	-	-	1	1.5	<b><math>2.5(2,1,3) \times 10^3</math></b>		-	
$\frac{3}{2}^+$	-	6.7931(17)	0	1.5	-		4.9(5)	
	<b>8.2866(2,10,1)</b>	8.2840(5)	0	1.5	<b>2.93(2,6,0)</b>		3.6(7)	
	-	-	2	1.5	<b>0.91(3,10,1)</b>		-	
	<b>9.5061(11,10,12)</b>	9.484(8)	2	0.5	<b>114.2(9,6,2)</b>		$\approx 200$	
	-	-	0	1.5	<b>158.7(11,11,14)</b>		-	
	<b>10.4971(21,20,16)</b>	10.506	2	0.5	<b>25.0(14,82,10)</b>		140(40)	
	-	-	0	1.5	<b>121(3,1,3)</b>		-	
	13	-	2	0.5	<b>830(110,240,80)</b>		-	
-	-	0	1.5	<b><math>3.51(6,310,16) \times 10^3</math></b>		-		
	-	-	2	1.5	<b><math>4.89(14,460,70) \times 10^3</math></b>		-	
$\frac{5}{2}^-$	<b>9.4852(2,10,1)</b>	9.488(3)	1	1.5	<b>7.3(2,10,0)</b>		10.1(5)	
	15	-	1	1.5	<b><math>4.0(2,6,3) \times 10^3</math></b>		-	
$\frac{5}{2}^+$	-	5.2409(3)	2	0.5	-		0.23	
	-	-	2	1.5	-		0.24	
	-	6.8594(9)	2	0.5	-		0.39(2)	
	-	-	2	1.5	-		0.42(2)	
	<b>8.9214(2,10,0)</b>	8.922(2)	2	1.5	<b>3.20(3,30,1)</b>		3.3(3)	
	<b>10.2691(5,20,2)</b>	10.3	2	1.5	<b>8.2(3,0,1)</b>		11(2)	
	15	-	2	0.5	<b><math>5.0(2,3,0) \times 10^3</math></b>		-	
$\frac{7}{2}^+$	-	7.2759(6)	2	1.5	-		1541(59)	
	<b>10.9063(8,20,6)</b>	10.917(12)	2	1.5	<b>85.1(7,2,6)</b>		90	

distributions for the two  $l = 2$  channels are similar, only the sum of their widths can be determined accurately. The uncertainty analysis results in a much improved estimate of the total proton width for this state and the branching between  $l = 0$  and 2 (see Table I).

To achieve the  $R$ -matrix fit shown in Figs. 4 and 7 a number of background poles were required to simulate the low energy tails of higher energy resonances. For the most part, these background poles are only needed to fit the data above  $E_{cm} = 3$  MeV. In particular, they are needed to fit the high energy side of the  $E_{cm} = 2.21$  MeV ( $J^\pi = 3/2^+$ ,  $E_x = 9.51$  MeV) resonance and the high-

est energy data near the resonance at  $E_{cm} = 3.60$  MeV ( $J^\pi = 7/2^+$ ,  $E_x = 10.91$  MeV). The quality of the fit was insensitive to the exact energy of all but the  $3/2^+$  background pole. The reduced widths of the  $3/2^+$  background pole were quite sensitive to its energy. In this regard, it is useful to compare the reduced widths from the fits with the corresponding Wigner limits (see, e.g. Ref. [32]). When the  $3/2^+$  background pole was placed at  $E_x = 15$  MeV, the fit resulted in values for the partial width that were much larger than the Wigner limit. If the pole was instead placed at a lower energy, the fitted widths were greatly reduced. Therefore, for the final fit,

the  $3/2^+$  background pole was placed at  $E_x = 13$  MeV. This sensitivity of the placement of the background pole suggests that there is a real broad  $3/2^+$  level(s) at energies just above the data. Indeed, Ref. [20] reports broad levels ( $\Gamma \approx 1$  MeV) given tentative spin assignments of  $(1/2, 3/2)^+$  at  $E_x = 13.45$  and  $15.10$  MeV. This is also consistent with  $R$ -matrix fits to the ground state capture data, which require a significant contribution from a  $3/2^+$  background pole (see Fig. 2).

To determine the branchings between channels of the same angular momentum but different intrinsic spin with greater sensitivity, polarization experiments could be performed but the number of observables that would likely need to be measured, the complexity of the analysis, and the lack of a low energy polarized beam facility makes this unlikely in the near future.

While the inelastic proton channel is also open at the highest energies ( $E_{cm} > 2.3$  MeV), inclusion of this channel in the calculations did not increase the quality of the fit. Inelastic protons were only observed in the experimental data at  $E_{cm} > 3.5$  MeV, confirming the small branching to this channel.

A preliminary multichannel  $R$ -matrix fit has been performed in order to illustrate the constraint of the scattering data on the capture data. Example data for the scattering channel (this work), ground state  $\gamma$  ray channel and  $E_x = 6.79$  MeV  $\gamma$  ray channel [10, 11, 19] are shown in Fig. 2 and were fit simultaneously. The  $^{14}\text{N} + p$  reactions represent a clear example of how the ANC can affect different reaction channels either as a subthreshold state (scattering or ground state  $\gamma$ -ray channel) or as the strength of the external capture ( $E_x = 6.79$  MeV  $\gamma$ -ray channel). The implementation of the ANC in  $R$ -matrix theory, to describe both of these reaction components, is given in detail in Ref. [33]. In Fig. 2 a) it is shown how the  $E_x = 6.79$  MeV subthreshold state makes a strong contribution to the scattering channel. While the scattering data cannot constrain the value of the ANCs as strongly as the transfer reactions, the measurements should be consistent, as is the case here. Further, by demonstrating that a simultaneous fit is achievable gives more confidence in the applicability of the phenomenological model.

An extrapolation of the  $S$ -factor for the ground state transition is shown in Fig. 2 b). This preliminary fit was performed by considering fixed normalizations for each of the data sets and is quite similar to that presented in Ref. [5] except with the inclusion of scattering data. To demonstrate the effect that the scattering data has on the fit, the uncertainty was first calculated using only the capture data. This was done using a Monte Carlo technique similar to that described in Ref. [34] except only point-to-point uncertainties were considered. As shown in Fig. 8 by the black outlined unfilled histogram, a bimodal probability density was produced corresponding to the tension between the energy dependence and normalizations of the different capture data sets. The red filled histogram shows the probability density resulting from the same fit but with the scattering data of this

work also included. The probability density is now constrained to a single peak that overlays the lower cross section peak of the calculation with out the scattering data. It is rather interesting to note that in the original calculation the higher cross section solution was significantly more probable.

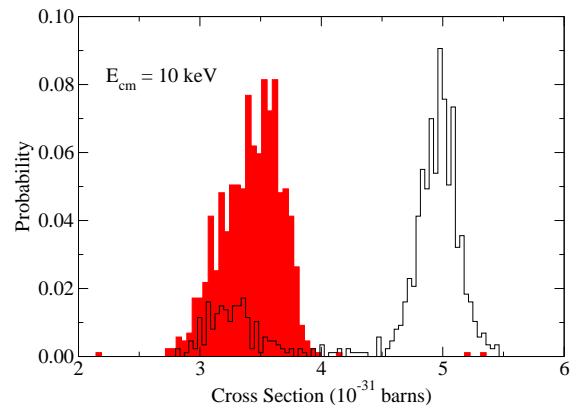


FIG. 8: (Color online) Example probability densities for the  $^{14}\text{N}(p, \gamma)^{15}\text{O}$  ground state transition cross section obtained from Monte Carlo uncertainty analyses. The black outlined unfilled histogram represents the result obtained when only the capture data from Refs. [10, 11, 19] were considered. The red solid histogram results when the scattering data of this work is also included.

While this demonstrates the significance of the scattering data, other uncertainties, like the sensitivity of the fit to the channel radius, background poles, experimental systematic uncertainties, and compatibility of the different capture data sets, are very significant and must be characterized before a new recommended value of the low energy  $S$ -factor can be given. To accomplish this, a detailed global analysis is in progress, which also includes newly measured capture data that cover the higher energy range [35]. These new capture data have been measured with the aim of improving on those of Ref. [19], where important summing corrections were neglected as discussed in Refs. [5, 11].

## V. SUMMARY

While several measurements exist for the  $^{14}\text{N}(p, p)^{14}\text{N}$  reaction, they are often inconsistent and many lack detailed uncertainties. A consistent set of yield ratio scattering data has been measured over the energy range  $0.9 < E_{cm} < 3.75$  MeV. The data strongly constrain the proton partial widths of resonances that contribute to the astrophysically important  $^{14}\text{N}(p, \gamma)^{15}\text{O}$  reaction, in particular the broad  $3/2^+$  resonance at  $E_{cm} = 2.21$  MeV. A preliminary multichannel  $R$ -matrix fit illustrates how the subthreshold states affect the scattering and capture data, mainly the  $E_x = 6.79$  MeV state. A preliminary uncertainty analysis demonstrates how the inclusion of

the scattering data leads to a more confident extrapolation of the ground state capture cross section. However, other uncertainty contributions remain, which are of equal or greater significance, that must be addressed through further capture and lifetime measurements.

### Acknowledgments

This research was supported in part by the Notre Dame Center for Research Computing and funded by the Na-

tional Science Foundation through Grant No. PHY-1068192, the Joint Institute for Nuclear Astrophysics Grant No. PHY08-22648, and in part by the US Department of Energy under contract No. DE-FG02-97ER41041.

- 
- [1] B. Aharmim, S. N. Ahmed, A. E. Anthony, N. Barros, E. W. Beier, A. Bellerive, B. Beltran, M. Bergevin, S. D. Biller, K. Boudjemline, et al. (SNO Collaboration), *Phys. Rev. C* **81**, 055504 (2010), URL <http://link.aps.org/doi/10.1103/PhysRevC.81.055504>.
- [2] G. Bellini, J. Benziger, D. Bick, S. Bonetti, G. Bonfini, M. Buizza Avanzini, B. Caccianiga, L. Cadonati, F. Calaprice, C. Carraro, et al. (Borexino Collaboration), *Phys. Rev. Lett.* **107**, 141302 (2011), URL <http://link.aps.org/doi/10.1103/PhysRevLett.107.141302>.
- [3] Borexino Collaboration, *Nature* **512**, 383 (2014), URL <http://dx.doi.org/10.1038/nature13702>.
- [4] W. Haxton, R. Hamish Robertson, and A. M. Serenelli, *Annual Review of Astronomy and Astrophysics* **51**, 21 (2013), <http://dx.doi.org/10.1146/annurev-astro-081811-125539>, URL <http://dx.doi.org/10.1146/annurev-astro-081811-125539>.
- [5] E. G. Adelberger, A. García, R. G. H. Robertson, K. A. Snover, A. B. Balantekin, K. Heeger, M. J. Ramsey-Musolf, D. Bemmerer, A. Junghans, C. A. Bertulani, et al., *Rev. Mod. Phys.* **83**, 195 (2011), URL <http://link.aps.org/doi/10.1103/RevModPhys.83.195>.
- [6] L. M. Krauss and B. Chaboyer, *Science* **299**, 65 (2003), <http://www.sciencemag.org/content/299/5603/65.full.pdf>, URL <http://www.sciencemag.org/content/299/5603/65.abstract>.
- [7] A. M. Lane and R. G. Thomas, *Rev. Mod. Phys.* **30**, 257 (1958), URL <http://link.aps.org/doi/10.1103/RevModPhys.30.257>.
- [8] P. Descouvemont and D. Baye, *Reports on Progress in Physics* **73**, 036301 (2010), URL <http://stacks.iop.org/0034-4885/73/i=3/a=036301>.
- [9] R. E. Azuma, E. Uberseder, E. C. Simpson, C. R. Brune, H. Costantini, R. J. de Boer, J. Görres, M. Heil, P. J. LeBlanc, C. Ugalde, et al., *Phys. Rev. C* **81**, 045805 (2010).
- [10] R. C. Runkle, A. E. Champagne, C. Angulo, C. Fox, C. Iliadis, R. Longland, and J. Pollanen, *Phys. Rev. Lett.* **94**, 082503 (2005), URL <http://link.aps.org/doi/10.1103/PhysRevLett.94.082503>.
- [11] G. Imbriani, H. Costantini, A. Formicola, A. Vomiero, C. Angulo, D. Bemmerer, R. Bonetti, C. Brogini, F. Confortola, P. Corvisiero, et al., *The European Physical Journal A - Hadrons and Nuclei* **25**, 455 (2005), ISSN 1434-6001, URL <http://dx.doi.org/10.1140/epja/i2005-10138-7>.
- [12] P. F. Bertone, Ph.D. thesis, The University of North Carolina at Chapel Hill (2010).
- [13] A. Gurbich, *Nuclear Instruments and Methods in Physics Research Section B: Beam Interactions with Materials and Atoms* **266**, 1193 (2008), ISSN 0168-583X, *ion Beam Analysis Proceedings of the Eighteenth International Conference on Ion Beam Analysis Eighteenth International Conference on Ion Beam Analysis*, URL <http://www.sciencedirect.com/science/article/pii/S0168583X07017235>.
- [14] D. Schürmann, R. Kunz, I. Lingner, C. Rolfs, F. Schümann, F. Strieder, and H.-P. Trautvetter, *Phys. Rev. C* **77**, 055803 (2008), URL <http://link.aps.org/doi/10.1103/PhysRevC.77.055803>.
- [15] K. Yamada, T. Motobayashi, H. Akiyoshi, N. Aoi, Z. Flp, T. Gomi, Y. Higurashi, N. Imai, N. Iwasa, H. Iwasaki, et al., *Physics Letters B* **579**, 265 (2004), ISSN 0370-2693, URL <http://www.sciencedirect.com/science/article/pii/S0370269303017477>.
- [16] P. F. Bertone, A. E. Champagne, D. C. Powell, C. Iliadis, S. E. Hale, and V. Y. Hansper, *Phys. Rev. Lett.* **87**, 152501 (2001), URL <http://link.aps.org/doi/10.1103/PhysRevLett.87.152501>.
- [17] A. M. Mukhamedzhanov, P. Bém, B. A. Brown, V. Burjan, C. A. Gagliardi, V. Kroha, J. Novák, F. M. Nunes, i. c. v. Piskoř, F. Pirlpesov, et al., *Phys. Rev. C* **67**, 065804 (2003), URL <http://link.aps.org/doi/10.1103/PhysRevC.67.065804>.
- [18] P. F. Bertone, A. E. Champagne, M. Boswell, C. Iliadis, S. E. Hale, V. Y. Hansper, and D. C. Powell, *Phys. Rev. C* **66**, 055804 (2002), URL <http://link.aps.org/doi/10.1103/PhysRevC.66.055804>.
- [19] U. Schröder, H. Becker, G. Bogaert, J. Görres, C. Rolfs, H. Trautvetter, R. Azuma, C. Campbell, J. King, and J. Vise, *Nuclear Physics A* **467**, 240 (1987), ISSN 0375-9474, URL <http://www.sciencedirect.com/science/article/pii/0375947487905288>.
- [20] F. Ajzenberg-Selove, *Nuclear Physics A* **523**, 1 (1991), ISSN 0375-9474, URL <http://www.sciencedirect.com/science/article/pii/037594749190446D>.
- [21] P. Tischhauser, A. Couture, R. Detwiler, J. Görres, C. Ugalde, E. Stech, M. Wiescher, M. Heil, F. Käppeler, R. E. Azuma, et al., *Phys. Rev. C* **79**, 055803 (2009), URL <http://link.aps.org/doi/10.1103/PhysRevC.79.055803>.
- [22] J. Keinonen and A. Anttila, *Comment. Physico-Math.* **46** (1976).
- [23] J. Hammer, W. Biermayer, T. Griegel, H. Knee, and

- K. Petkau, *RHINOCEROS, the Versatile Stuttgart Gas Target Facility (Part I)*, unpublished.
- [24] M. Jaeger, R. Kunz, A. Mayer, J. W. Hammer, G. Staudt, K. L. Kratz, and B. Pfeiffer, *Phys. Rev. Lett.* **87**, 202501 (2001), URL <http://link.aps.org/doi/10.1103/PhysRevLett.87.202501>.
- [25] K. Wolke, V. Harms, H. Becker, J. Hammer, K. Kratz, C. Rolfs, U. Schröder, H. Trautvetter, M. Wiescher, and A. Wöhr, *Zeitschrift für Physik A Atomic Nuclei* **334**, 491 (1989), ISSN 0939-7922, URL <http://dx.doi.org/10.1007/BF01294757>.
- [26] R. J. deBoer, A. Couture, R. Detwiler, J. Görres, P. Tischhauser, E. Uberseder, C. Ugalde, E. Stech, M. Wiescher, and R. E. Azuma, *Phys. Rev. C* **85**, 045804 (2012), URL <http://link.aps.org/doi/10.1103/PhysRevC.85.045804>.
- [27] AZURE2 *R*-matrix code, URL [azure.nd.edu](http://azure.nd.edu).
- [28] C. R. Brune, *Phys. Rev. C* **66**, 044611 (2002), URL <http://link.aps.org/doi/10.1103/PhysRevC.66.044611>.
- [29] F. James and M. Roos, *Computer Physics Communications* **10**, 343 (1975), ISSN 0010-4655, URL <http://www.sciencedirect.com/science/article/pii/0010465575900399>.
- [30] W. Press, S. Teukolsky, W. Vetterling, and B. Flannery, *Numerical Recipes: The Art of Scientific Computing* (Cambridge University Press, 32 Avenue of the Americas, New York, NY 10013-2473, USA, 2007), 3rd ed.
- [31] C. Angulo and P. Descouvemont, *Nuclear Physics A* **690**, 755 (2001), ISSN 0375-9474, URL <http://www.sciencedirect.com/science/article/pii/S0375947400006965>.
- [32] C. E. Rolfs and W. S. Rodney, *Cauldrons in the Cosmos* (The University of Chicago Press, Chicago, 1988), 1st ed.
- [33] A. M. Mukhamedzhanov and R. E. Tribble, *Phys. Rev. C* **59**, 3418 (1999), URL <http://link.aps.org/doi/10.1103/PhysRevC.59.3418>.
- [34] R. J. deBoer, J. Görres, K. Smith, E. Uberseder, M. Wiescher, A. Kontos, G. Imbriani, A. Di Leva, and F. Strieder, *Phys. Rev. C* **90**, 035804 (2014), URL <http://link.aps.org/doi/10.1103/PhysRevC.90.035804>.
- [35] Q. Li, J. Görres, R. J. deBoer, G. Imbriani, A. Best, A. Kontos, P. J. LeBlanc, E. Uberseder, and M. Wiescher, in preparation.